DESIGN AND FABRICATION OF A SINGLE-LAYER GUIDED MODE RESONANCE GRATING TRANSMISSION FILTER

BY

MAANAV S. GANJOO

THESIS

Submitted in partial fulfillment of the requirements
for the degree of Master of Science in Electrical and Computer Engineering
in the Graduate College of the
University of Illinois Urbana-Champaign, 2021

Urbana, Illinois

Adviser:

Professor John Dallesasse

ABSTRACT

To improve upon a multi-layer linear variable filter used as a spectral analyzer in a previous microfluidic lab-on-a-chip viral diagnosis assay, a single-layer spectral analyzer is envisioned. The device uses the guided mode resonance effect, which has been used in the past to make optical stopband filters that only reflect a very narrow range of wavelengths. It has been shown that these filters can be designed to reflect an arbitrarily narrow range of wavelengths, if designed correctly. In this work, the same phenomenon is exploited to design an optical passband filter, using a simple, single-layer design, which only transmits a narrow range of wavelengths.

To accomplish this, a discussion of the guided mode resonance effect and its more general form (the Wood's anomaly) is included. This discussion throws light on the nature of the optical phenomenon which relies on the excitation of leaky modes on the grating surface, with the anomalous transmission or reflection resulting from the coupling of incident light to these modes.

The envisioned design requires the preparation of a high index, optically transmissive thin film on a low index substrate. The semiconductor gallium phosphide (GaP) is chosen for its high index and transmissivity over its bandgap (549 nm). Since depositing GaP on glass using CVD would be difficult, the thin film is prepared by ion implanting a GaP wafer with a high dose of helium and bonding to borosilicate glass. It is seen that the surface of the implanted GaP adheres strongly to the glass and separates from the substrate, leaving a thin film with a consistent thickness and an rms roughness of around 10 nm.

Gratings are defined using an electron beam lithography technique. Three etch chemistries were tried to etch the thin film, starting with Cl_2 and BCl_3 only. The etch was found to be too fast and isotropic, so a O_2 was added to dilute the etch gasses. However, this resulted in undesirable micromasking, so a BCl_3, Cl_2, H_2 and CH_4 mixture was used, which was found to have the slowest etch rate and the least micromasking, at the cost of a low selectivity against PECVD SiO_2 and SiN masks.

The finished gratings are tested using visible spectrophotometry and the results are shown to be far inferior to the simulations. This is likely due to the sensitivity of the simulated design, resulting from instability due to the low reflection coefficient of the GaP-glass interface. An alternate design using a metal-on-waveguide design is suggested for its higher background reflectivity.

To everyone who has lost any sleep to make my education and research possible.

ACKNOWLEDGMENTS

My first and biggest thanks goes to John A. Carlson, my friend and mentor, who put in many hours coaching me and pushing me to be my best. Without his guidance and mentorship, I might not be half the researcher I am today.

I would like to thank my teammates Patrick Su, Robert B. Kaufman and Kevin P. Pikul for all the advice and intellectual discussion which helped me develop my understanding of my work.

I would like to thank Professor John M. Dallesasse, who worked tirelessly behind the scenes so that I could focus on my research and who gave me the opportunity to fall in love with the field of semiconductor fabrication as an undergraduate researcher. Without his guidance and support I would not have come nearly as far I did.

I must thank Joseph W. Maduzia, Dr. Kaicheung Chow and Lavendra Mandyam, who took time from their busy schedules to help me advance my work, alongside Dr. Mark J. McCollum, Yanguang Lian, Paul S. DiPippo, Dr. Julio A. N. D. Soares and Dr. Kathy Walsh who worked hard to maintain lab resources essential to my work.

I would like to acknowledge the various research units at the University of Illinois that facilitated my research and the work of many others now and before me. These include the Holonyak Micro- and Nanotechnology Lab, the Micro- and Nanomechanical Systems Lab and the Frederick Seitz Materials Research Lab.

Finally, I would like to thank my family and the University of Illinois for providing me the opportunity to learn from and be inspired by the works of many other researchers pushing the boundaries of our knowledge every day.

CONTENTS

LIST OF ABBREVIATIONS vi

CHAPTER 1 MOTIVATION 1
1.1 The ELISA Process 2
1.2 LVF Design 3

CHAPTER 2 FROM WOOD'S ANOMALIES TO GUIDED MODE RESONANCE FILTERS 4
2.1 A Brief Overview of Wood's Anomalies 4
2.2 GMR Theory - Principle of Operation 6
2.3 Transmissive GMR Filters 9
2.4 Suggested Single-Layer GMR Filter Design 11

CHAPTER 3 DESIGN AND FABRICATION 13
3.1 Device Simulations and Optimization 13
3.2 Layer Transfer 16
3.2.1 Anodic Bonding Theory 16
3.2.2 Past Work in Anodic Bonding 19
3.2.3 Ion Implant and Exfoliation 19
3.3 Implant and Bonding Parameters 21
3.3.1 Results of Layer Transfer 23
3.4 Etching of Gratings 24
3.5 Transmission Spectra of Fabricated Gratings 27

CHAPTER 4 CONCLUSION AND FUTURE WORK 29

REFERENCES 30

LIST OF ABBREVIATIONS

DBR	Distributed Bragg Reflector
DE	Diffraction Efficiency
ELISA	Enzyme-Linked Immunosorbent Assay
GMR	Guided Mode Resonance
ICP	Inductively Coupled Plasma
IR	Infra-Red
LOC	Lab-on-a-Chip
PECVD	Plasma Enhanced Chemical Vapor Deposition
RCWA	Rigorous Coupled Wave Analysis
RCWT	Rigorous Coupled Wave Theory
RIE	Reactive Ion Etch
SRIM	Stopping Range of Ions in Matter
TRIM	Transmission Range of Ions in Matter

CHAPTER 1
MOTIVATION

Advancements in biochemical assays and microfluidic technology have allowed for the development of potent lab-on-a-chip (LOC) systems with the ability to run complex assays with significant savings in cost, time, and complexity. This has allowed for the development of cheap, portable systems capable of detecting viral infections in patients using small quantities of the patient's body fluids, usually blood. These techniques could prove vital for increasing rapid testing capabilities for highly infectious viruses like the human immunodeficiency virus, severe acute respiratory syndrome virus and the zika virus which are major concerns to global health.

In work preceding this thesis [1], an LOC system was envisioned by the Cunningham group at the University of Illinois based on an enzyme-linked immunosorbent assay (ELISA). The assay worked by diluting a small amount of blood and causing a visible color change if virus antigen particles were detected. The novelty of this technique was that the color change could be quantified by taking a picture of the setup through a smartphone camera and using image processing techniques to determine if the change was strong enough. The technique relied on the use of a modified Fabry-Perot filter as a spectral analyzer. This thin film narrow-band optical transmission filter is modified so that the central wavelength of the transmission band varied linearly across the length of the device, allowing it to act as a spectral analyzer and opening the door for the LOC technique to be used with a broader set of color changes.

The primary limitation of this LVF was that it relied on a multi-layered distributed Bragg reflector (DBR) stack, the fabrication of which is complex and expensive. This is antithetical to the assay being developed, which is supposed to be simple and cheap. For this reason, a new single-layer LVF was envisioned to replace the Fabry-Perot LVF. This thesis follows the design optimization and fabrication process for this LVF.

1.1 The ELISA Process

The ELISA technique was developed by Engvall and Perlmann [2] as a means of quantifying the concentration of antigens and antibodies in sample tissue, which is an essential step in studying the immune response of living matter. This technique has now been widely adopted and coupled with microfluidic systems to enable highly sensitive and quantitative detection of immune responses in people experiencing viral infections and allergic reactions.

While there are numerous developments that improve and optimize the assay, most ELISAs follow four common steps which are (i) surface functionalization, (ii) analyte capture, (iii) analyte detection, and (iv) signal amplification.

In the first step, the antigen being quantified is determined and a suitable antibody with a high capture efficiency for the antigen is selected. A fluid channel is made in a polymer material, to act as a reacting surface. A suspension of the antibody is prepared in which an added chemical group on the antibody will react with the polymer surface and affix the antibody molecules to it. It is vital that the antibody molecules strongly fix onto the surface so that when the antibody suspension is washed out of the channel, only the antibodies fixed to the surface remain. Additionally, the fixation process must orient the antibodies with their capture sites facing away from the surface and towards the center of the channel, to maximize the capture efficiency in the next step.

Next the analyte solution containing an unknown quantity of antigen is flowed into the channel and allowed to sit. In this time, antigen particles in the solution diffuse around the channel and, upon encountering antibodies at the surface, will bind to the antibodies. After an empirically optimized time, this channel is again washed so that some antigen remains bound to the surface.

In the third step, a suspension of detection antibodies is prepared and introduced to the channel. These antibodies are nearly identical to the capture antibodies except that, instead of a chemical group meant to bind them to the surface, they are linked to an enzyme. When these detection antibodies encounter antigen bound to the channel surface, they bind to these antibodies and remain on the surface after it is washed one last time.

Finally, a signal solution is introduced to the channel. This solution contains a reagent that reacts in the presence of the enzyme introduced in step (iii) to cause some measurable change, usually in color. This step is the key strength of the ELISA process, because the signal strength (usually intensity of color change) is a function of the concentration of the antigen being quantified and the time the signal solution sits in the channel. This gives well-designed ELISAs very large dynamic ranges, as the intensity of the

color change is magnified with time allowing for low limits of detection and quantification at longer time scales, while preserving sensitivity at high antigen concentrations at shorter time scales.

1.2 LVF Design

The LVF used in the previous work was a commercially designed device whose exact structure is not known. However, some general principles for the design of Fabry-Perot LVFs are well understood [3].

The simplest DBR LVF consists of an airgap cavity sandwiched between two DBR mirrors. The high reflectivity of the DBR mirrors creates strong Fabry-Perot interference in the cavity, so that only light that constructively interferes after travelling the length of the cavity (so that the wavelength is a multiple of twice the cavity thickness) makes it through. All other wavelengths rapidly destructively interfere and do not pass through the device. Not only is this device easy to design, it is also easy to convert into an LVF by simply varying the thickness of the cavity linearly along the filter length [4].

While DBR based LVFs can give very narrow linewidths, this requires that the DBR mirrors have very high reflectivity. To achieve this high reflectivity, very thick stacks, sometimes exceeding 20 layers, must be used. This increase in the number of layers correlates with an increase in device complexity and price, which presents a problem in reducing the cost of the antigen assay.

For this reason, an alternate filter design that relies on the guided mode resonant effect was suggested. This effect presents as rapid fluctuations in the transmission properties of ruled gratings which, crucially, do not require more than three or four layers. Chapter 2 elaborates on the nature of this phenomenon and Chapter 3 describes the design and fabrication of this device.

CHAPTER 2
FROM WOOD'S ANOMALIES TO GUIDED MODE RESONANCE FILTERS

The guided mode resonance (GMR) effect was proposed in 1965 by Hessel and Oliner [5], even before it was called the GMR effect, to more fully explain the existence of so-called "Wood's anomalies" [6]. These anomalies are observed as sudden changes in transmission/reflection intensity in the spectrum of a parallel grating. Over the years, this phenomenon has been exploited to create simple high-reflective or transmissive structures as well as narrow-band filters.

2.1 A Brief Overview of Wood's Anomalies

In 1902, Robert Wood [6] noted that the transmission and reflection spectrum of parallel metal grating structures contained abrupt changes in intensity that were hitherto unexplained. These echelette gratings were fabricated by means of scratching grooves, at a number density of in the range of 5000 to 15,000 grooves per inch, into a metal thin film on a non-metallic substrate with a diamond tip. Wood observed that these gratings displayed narrow light and dark bands when illuminated by an incandescent lamp (Figure 1), as was expected. However, he noted that, at certain incident angles, bright and dark bands appeared which were so narrow as to "show one of the D lines, and not the other" referring to the two sodium lines at 589 nm and 589.6 nm in the Fraunhofer series. This implied that the grating's spectral response varied very rapidly (high-transmission to low-transmission in under 0.6 nm) at some regions in the spectra which was, crucially, much faster than the contemporaneous theory on grating response predicted. Additionally, these "anomalous" bands were stronger when incident light was s-polarized (E-field perpendicular to the gratings) and disappeared altogether when the incident light was p-polarized (E-field parallel to the gratings).

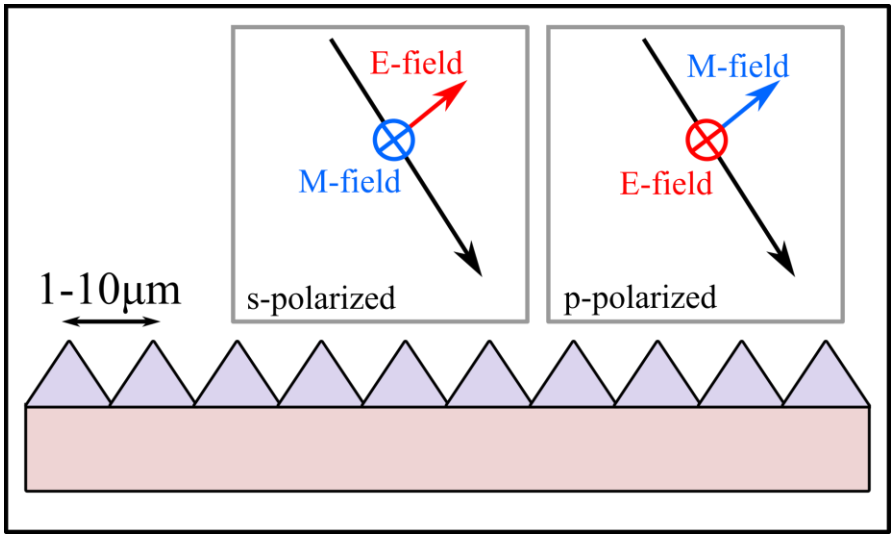

Figure 1: Diagram showing cross section of gratings observed by Wood. The insets show the orientation of the electric field, with respect to the gratings, for s-polarized and p-polarized light.

This phenomenon was investigated by numerous authors with only moderate success, until Lord Rayleigh [7] proposed a mechanism for their formation in 1907. Rayleigh made an analogy to earlier works involving the scattering of sound waves by a subwavelength aperture, extending these works to consider the reflection of sound by an infinite linear array of such apertures. In doing so, he showed that similar arguments could be made for an infinite series of parallel gratings and was able to predict both the wavelengths at which the bright anomalies occurred, as well as their polarization dependence. However, the theory failed to account for dark anomalies and the precise form of the spectral response the anomalies presented. Others would work to improve on Rayleigh's scattering approach, but none could explain every aspect of Wood's observations.

In 1952, Palmer [8] demonstrated Wood's-like anomalies in ruled gratings illuminated with p-polarized light, violating previous hypotheses. In doing so, he pointed out that grating shape had a crucial role to play in the spectral response of the grating, remarking that in experiments where p-anomalies where wholly absent, shallow gratings had been used, as opposed to the "deeply ruled" gratings used in his experiment. As such, s-type anomalies (henceforth called Rayleigh anomalies) and p-type anomalies (henceforth called Palmer anomalies) can be simultaneously present, although shallow ruling of gratings tends to eliminate Palmer anomalies entirely. Since all previous theories relied on the assumption of shallow ruled gratings, it was clear that a new theory would be needed to explain Palmer anomalies.

In the introduction to his 1952 paper, Palmer [8] suspected that Palmer anomalies were not a result of Rayleigh scattering but some underlying resonance phenomena. However, it was not until 1965 that the

first robust resonance approach was published by Hessel and Oliner [5]. In their paper they noted two types of anomalies, the first of which presented itself upon the onset or disappearance of a new diffraction order in the gratings. The onset of these diffraction orders corresponds exactly to the various scattering orders discussed by Rayleigh and, hence, corresponds to the location of Rayleigh anomalies. More importantly, Hessel and Oliner's work examined a second type of anomaly which resulted from the grating being able to support various "leaky" modes which were excited when either the reflected beam or one of the diffracted beams was incident at the same angle as would be taken by the leaky mode.

Wang and Magnusson [9], along with coauthors Bagby and Moharam, further developed Hessel and Oliner's work in 1990, coining the term "guided mode resonance" to refer to the Palmer anomalies. Using rigorous coupled wave theory, they were able to solve for the reflectance and transmittance of light incident on a planar dielectric waveguide with modulated reactance, noting ironically that the waveguide cannot support guided modes because of the several externally propagating diffracted orders. In fact, the anomalies presented sharp variations in transmittance and reflectance precisely because of this fact and would have shown smooth variation if the incident light was exciting truly guided modes, like smooth Fabry-Perot modes that would have been excited in an unmodulated waveguide.

2.2 GMR Theory - Principle of Operation

Wang et al. [9] go through a simple, yet powerful discussion of the GMR phenomena using rigorous coupled wave theory in their 1990 paper. The discussion begins by positing a "symmetric" planar waveguide (Figure 2). This waveguide is so named because permittivity of the regions before and after the grating are identical, resulting in a symmetrical spectral response, as shown in Figure 3. The permittivity of the symmetric planar waveguide is spatially modulated in the following manner:

$$\epsilon_2(x) = \epsilon_0 + \Delta\epsilon \cos Kx \tag{1}$$

Here, ϵ_2 is the permittivity of the waveguide layer at location x, ϵ_0 and $\Delta\epsilon$ correspond to the average permittivity and the amplitude of the permittivity variation respectively, and K is a wavenumber that can be calculated using $K = 2\pi/\Lambda$ where Λ is the period (Figure 2) of the gratings.

Assuming the grating material is lossless, and we are interrogating the surface with an obliquely incident p-polarized plane wave, we can write the wave equation as follows:

$$\nabla^2 E_y(x,z) = -k^2 \epsilon_2(x) E_y(x,z) \tag{2}$$

Here, E_y is the total electric field and k is the free-space wavenumber of the incident wave.

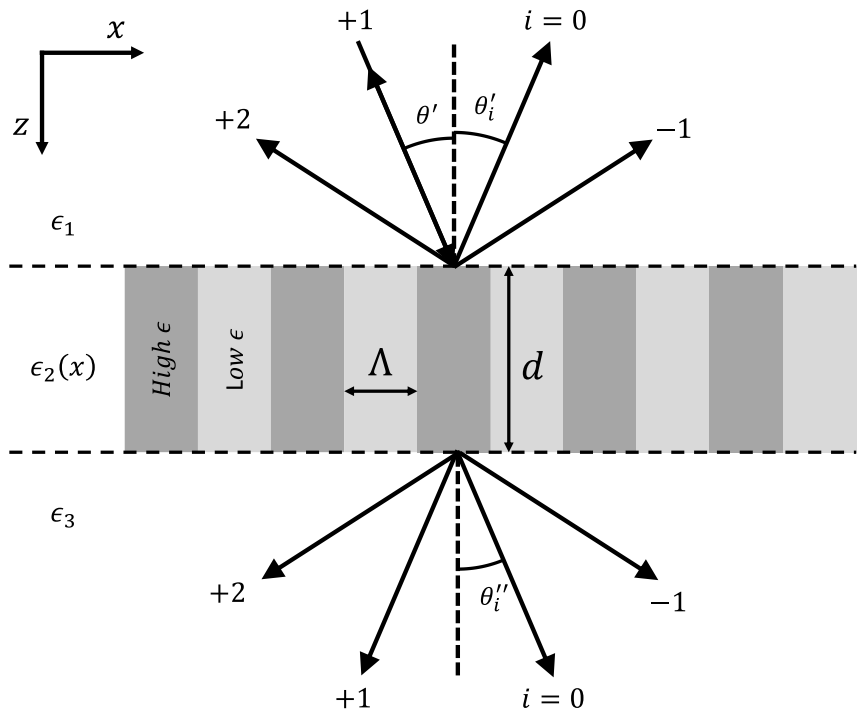

Figure 2: Diagram representing symmetric GMR filter proposed by Magnusson and Wang, along with various symbols used in its analysis. [5]

Because ϵ_2 varies periodically, we may use Floquet's theorem to write the general solution of $E_y(x,z)$ as follows:

$$E_y(x,z) = \sum_{i=-\infty}^{\infty} S_i(z)\exp\left(-j\boldsymbol{\sigma}_i \cdot \boldsymbol{r}\right) \tag{3}$$

Here $\boldsymbol{\sigma}_i = (k_{2x} - iK)\hat{x} + (k_{2z})\hat{z}$ defined by the vector Floquet condition, and k_{2x} and k_{2y} are the x and y components, respectively, of the wave vector of the zeroth-order space-harmonic component having a magnitude of $k_2 = k\sqrt{\epsilon_0}$ so that $k_{2x} = k_2 \sin\theta$ and $k_{2z} = k_2 \cos\theta$ with θ being the internal reflection angle associated with zeroth-order space-harmonic.

Substituting the Floquet expansion (3) into the wave equation (2) and expanding using Euler's equation gives:

$$\frac{1}{2\pi^2}\frac{d^2S_i(z)}{dz^2} - j\frac{2}{\pi}\left(\frac{\sqrt{\epsilon_0}\cos\theta}{\lambda}\right)\frac{dS_i(z)}{dz} + \frac{2i(m-i)}{\Lambda^2}S_i(z) + \frac{\Delta\epsilon}{\lambda^2}\left[S_{i-1}(z) + S_{i+1}(z)\right] = 0 \tag{4}$$

Here, $m = 2\Lambda\sqrt{\epsilon_0}\sin(\theta/\lambda)$.

Additionally, the E-fields at the incident and reflecting sides are given by:

$$E_1 = \exp(-j\boldsymbol{k}_1 \cdot \boldsymbol{r}) + \sum_{i=-\infty}^{\infty} R_i \exp\left(-j\boldsymbol{k}_{1i} \cdot \boldsymbol{r}\right) \tag{5}$$

$$E_3 = \exp(-j\boldsymbol{k}_3 \cdot \boldsymbol{r}) + \sum_{i=-\infty}^{\infty} T_i \exp\left(-j\boldsymbol{k}_{3i} \cdot (\boldsymbol{r} - d\hat{z})\right) \tag{6}$$

Here, R_i and T_i are the reflected wave amplitude in region 1 and transmitted wave amplitudes in region 3 (Figure 2) respectively. $\boldsymbol{k}_{1i}$ and $\boldsymbol{k}_{3i}$ are the wavenumbers of the incident and transmitted waves respectively and d is the thickness of the filter in the z axis.

Solving for S_i, R_i and T_i is an involved process that cannot be sufficiently covered in this thesis. However, Gaylord and Moharam [10] develop an exhaustive analysis in their 1965 paper.

By applying the continuity and differentiability boundary conditions at z = 0 and z = d, four sets of linear equations are obtained which can be solved simultaneously for the diffraction efficiency in region 1, DE_1 (how strongly power is reflected by the grating) and the diffraction efficiency in region 3, and DE_3 (how strongly power is transmitted by the grating):

$$DE_{1i} = Re\left[\frac{\boldsymbol{k}_{1i} \cdot \hat{\boldsymbol{z}}}{\boldsymbol{k}_{10} \cdot \hat{\boldsymbol{z}}}\right] |R_i|^2 \tag{7}$$

$$DE_{3i} = Re\left[\frac{\boldsymbol{k}_{3i} \cdot \hat{\boldsymbol{z}}}{\boldsymbol{k}_{10} \cdot \hat{\boldsymbol{z}}}\right] |T_i|^2 \tag{8}$$

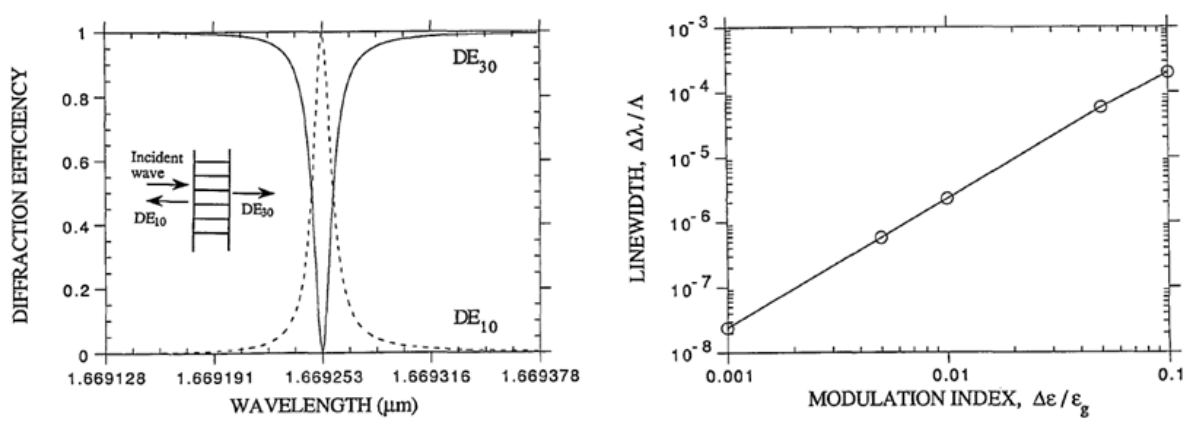

Figure 3: (left) Simulated spectral response of symmetric GMR filter. (right) Calculated linewidth of filter plotted as a function of modulation index. [7]

The GMR effect can be exploited to engineer high-reflective gratings with a very narrow bandwidth. In further work by Wang and Magnusson [11] it is seen that for a thin-film dielectric grating with modulated permittivity, in the limit of little to no modulation, the bandwidth of the reflective anomaly can be made arbitrarily small by reducing the modulation amplitude $\Delta\epsilon$. This, coupled with the fact that GMR filters are relatively simple to fabricate, since they only consist of one etched film on a substrate, makes the GMR filter a useful tool in a variety of applications. Wang and Magnusson proposed four applications for such a filter. These include (a) a narrowband, high-reflective, polarized mirror for lasers, (b) a mirror for a tunable polarized laser, (c) a photorefractive tunable filter and (d) an electrooptic switch. While most of these devices are not common in the literature, they demonstrate the niche potential of the GMR grating.

2.3 Transmissive GMR Filters

So far, all the applications of GMR filters explored in this thesis rely on their high-efficiency, narrow-band reflectivity. However, from Wood's paper over a century ago, it is clear that Wood's anomalies come in both reflective and transmissive variants. This opens the possibility of using GMR gratings as narrowband *transmission* filters.

However, this requires a fundamentally different approach to GMR filter design than what is shown in Wood's paper. In 1995, Magnusson and Wang [11] explored this idea by simulating the effects of a multilayered GMR design using rigorous coupled wave theory (RCWT). They found that, while single-layer *reflection* filters made using the GMR effect had high-efficiency and narrow linewidth, single-layer *transmission* filters using the same basic structure tended to have poor efficiency and broad linewidth. This can be seen in (Figure 4). The top-right spectral response comes from a simulated two-layer GMR filter. While there is a clear transmission peak, the peak to background ratio of the filter is poor. This is because the optical properties of a GMR filter resemble those of the material stack they are defined in sans gratings.

Since it is difficult to make a high reflective dielectric surface without including multiple layers, gratings with few layers tend to have higher background transmittance. As more layers are added to the GMR, the peak to background ratio improves (Figure 4: 8 layers at bottom left and 11 layers at bottom right). This is because the increased number of layers allows for higher background transmittance using a DBR-like structure. However, doing so does increase the complexity of the device, reducing the ease of fabrication, which is a primary strength of the conventional GMR reflection filter.

Since then, there have been numerous attempts to use optical gratings as transmission filters, such as the work by Kanamori et al. [12] to make silicon on quartz color filters for use in pixels. However, their

objective aligned with a more broad-band transmission response and they were more concerned with suppressing higher order lines, so they were not plagued by the limitations of the simple GMR filter.

Song et al. [13] managed to get narrow linewidth transmission filters in the far IR frequencies by fabricating their gratings using a metal grating evaporated onto a dielectric waveguide. By not limiting themselves to dielectrics, they were able to get high reflectance without using a multilayered structure, since metal thin films have high reflectance if the metal layer is thicker than the skin depth of the incident light and the fill factor of the grating is high. Conversely, the use of metals resulted in significant signal loss near the resonance wavelength due to the high conductivity of the metals. These losses limit the transmission efficiency of the filter.

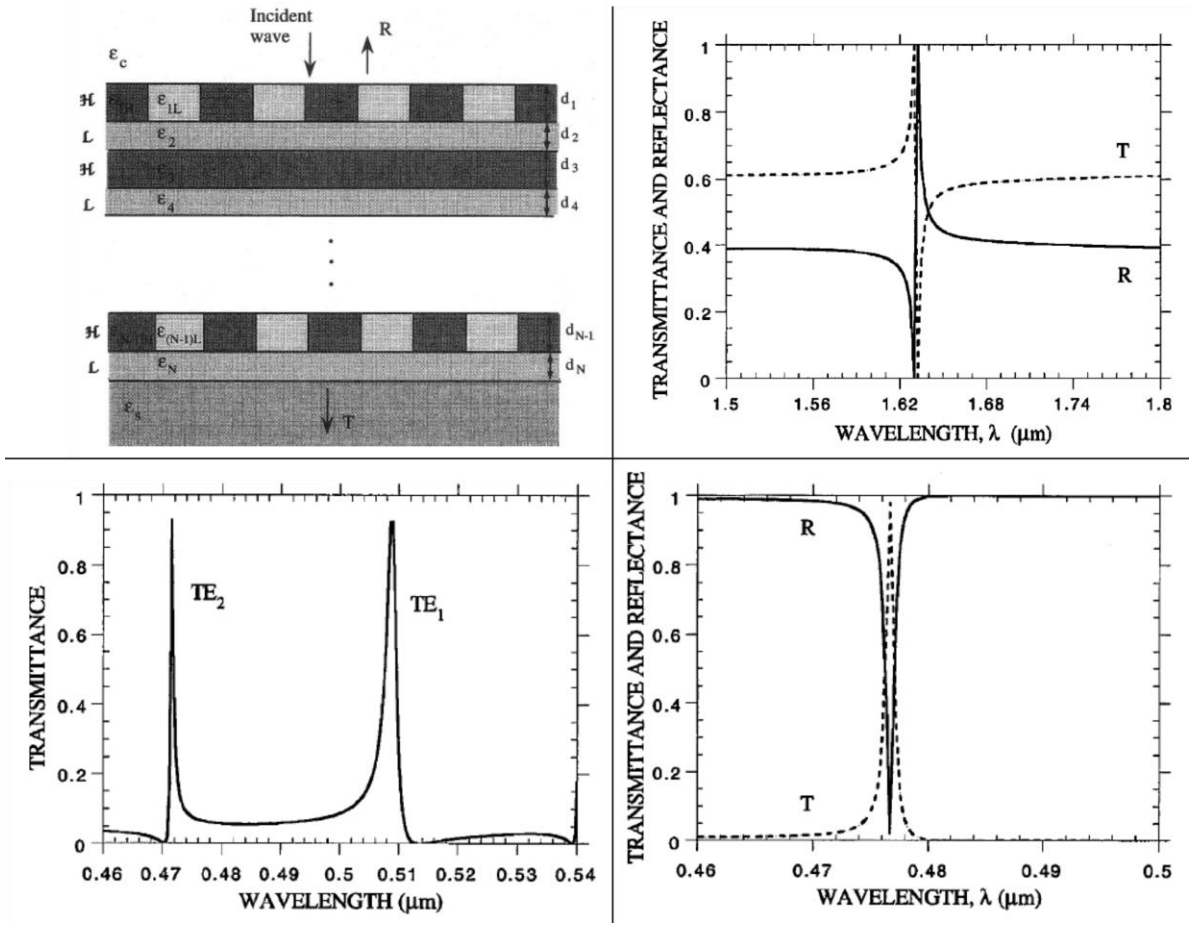

Figure 4: Schematic of general multi-layer GMR filter layout in Magnusson and Wang's [14] analysis (top left), accompanied by spectral responses for transmission filters with only 2 layers (top right), 8 layers, with 1st and 7th layer modulated (bottom left) and 11 layers, with 1st and 11th layer modulated (bottom right).

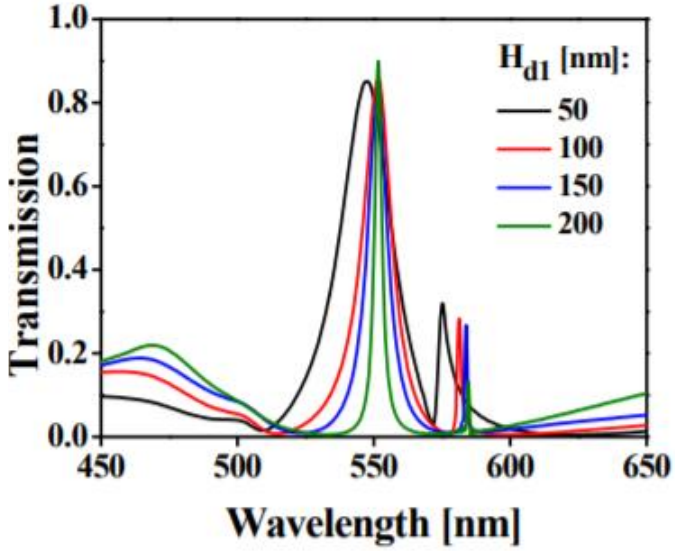

Figure 5: Transmission spectra of gratings for TE and TM polarized incident light, at various waveguide indices. [12]

Park et al. [14] went a step further and developed 2-D patterned metal gratings on a dielectric waveguide structure that gave much more desirable transmission properties (Figure 5). These devices were made by patterning a square lattice into a metal thin film on a SiO_2, SiN waveguide and had the added benefit of increasing the device's symmetry and reducing the effect of polarization on the transmission properties.

As such, any work trying to improve on the GMR filter will have to increase the number of adjustable variables, either by adding more layers to the structure or by increasing the complexity of the grating geometry itself. While the latter does not directly increase the cost of the device as significantly, it does make the device harder to design outside of simple cases like Park et al. and risks an increase in contamination by higher diffraction orders. In this work, a new design is proposed that addresses the issue of the poor background spectra while not significantly increasing complexity.

2.4 Suggested Single-Layer GMR Filter Design

As discussed earlier, GMR filter design begins by designing a thin film stack with desirable background transmission and reflection properties and then introducing appropriate periodic grating in the structure. If designed correctly, this periodicity will cause incident light of only certain fields to couple into modes supported by the grating, which will cause the transmission and reflection characteristics to "flip" at that frequency. Thus, one of the primary complications when designing a single-layer transmission GMR filter is devising a highly reflective thin film with only a single layer. This requires a material with a high

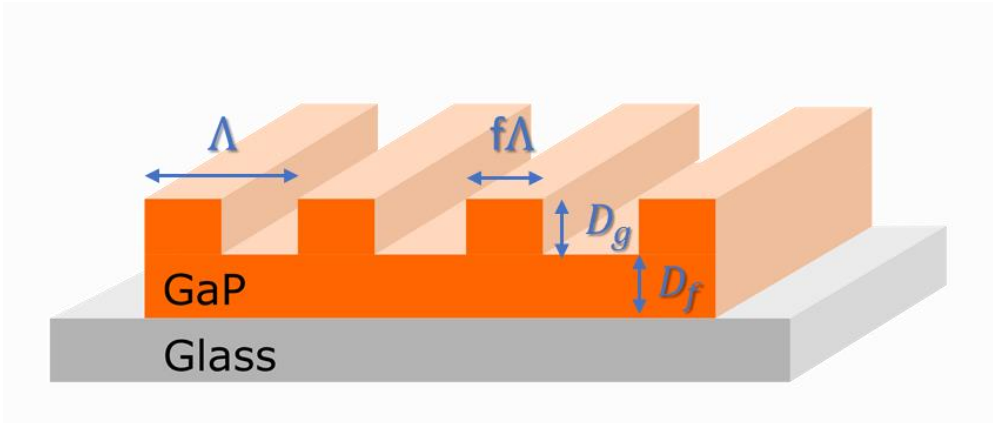

Figure 6: Basic structure of GaP on glass GMR gratings. Λ is the grating period, f is the "fill-factor" or the portion of the period that is un-etched, D_g is the etch-depth of the grating and D_f is the thickness of the unetched portion of the GaP thin film, referred to as the filler depth.

refractive index, to give a high reflection coefficient, but most common dielectrics do not have refractive indices greater than 2. Additionally, using metals limits the transmission efficiency due to the lossy coupling of transmitted light into the metal.

This work suggests the use of gallium phosphide (GaP) for use in a visible spectrum transmissive GMR filter. GaP is a semiconductor with a refractive index exceeding 3 in the visible range and low absorption for light of energy lower than its bandgap energy of 2.26 eV (wavelength greater than 549 nm). By etching gratings into a GaP film on a low index substrate, a background reflection coefficient as high as 55% is achieved, compared to the roughly 40% achieved by Magnusson and Wang's [15] single-layer transmission design.

The basic device structure is shown in Figure 6. The device was designed by varying D_g, D_f and f and checking the transmission spectra using an RCWA solver. Once this is done, Λ is varied for fine control of the location of the resonance peak, within a short wavelength range. This process is elaborated on in Section 3.1.

CHAPTER 3
DESIGN AND FABRICATION

The device design presented in section 2.4 requires a thin film of GaP to be deposited on a glass substrate, which would be difficult to do using an MOCVD system. To simplify this process, this work implements a layer transfer method similar to the Smart Cut method [16] for the production of silicon-on-insulator thin films that allows for the fabrication of a gallium phosphide thin film, with preliminary results presented at the CSMANTECH conference [17].

With this technology, the fabrication flow can be summarized in the following manner (Figure 7). First, a 50 mm GaP wafer is ion implanted with He^+ to create a subsurface layer of GaP supersaturated with He. The implanted side was anodically bonded to a glass wafer causing the He atoms to congregate and exfoliate the GaP wafer. This caused the wafer to separate from the thin film which was left bonded to the glass substrate. A hard-mask was deposited, and E-beam lithography was used to draw the grating pattern on the sample, which was etched into the hard-mask. Finally, a plasma etch was used to remove the hard-mask and get the finished devices. The rest of this chapter elaborates on the processes used and how they were optimized.

3.1 Device Simulations and Optimization

The simulations in this work were carried out in the Diffract MOD module of the RSOFT suite developed by Synopsis. Diffract MOD solves problems using an RCWA solver, which divides the space into several regions and expands the field functions in each region using Floquet's theorem. Modes can then be calculated inside each region and the coupling of modes in adjacent regions can then be solved for to get an infinitely large linear system of equations. To truncate the problem, higher order functions in the Floquet expansion are cut off and the system is solved. For a more detailed explanation, the author recommends Moharam and Gaylord's analysis on a planar grating [18].

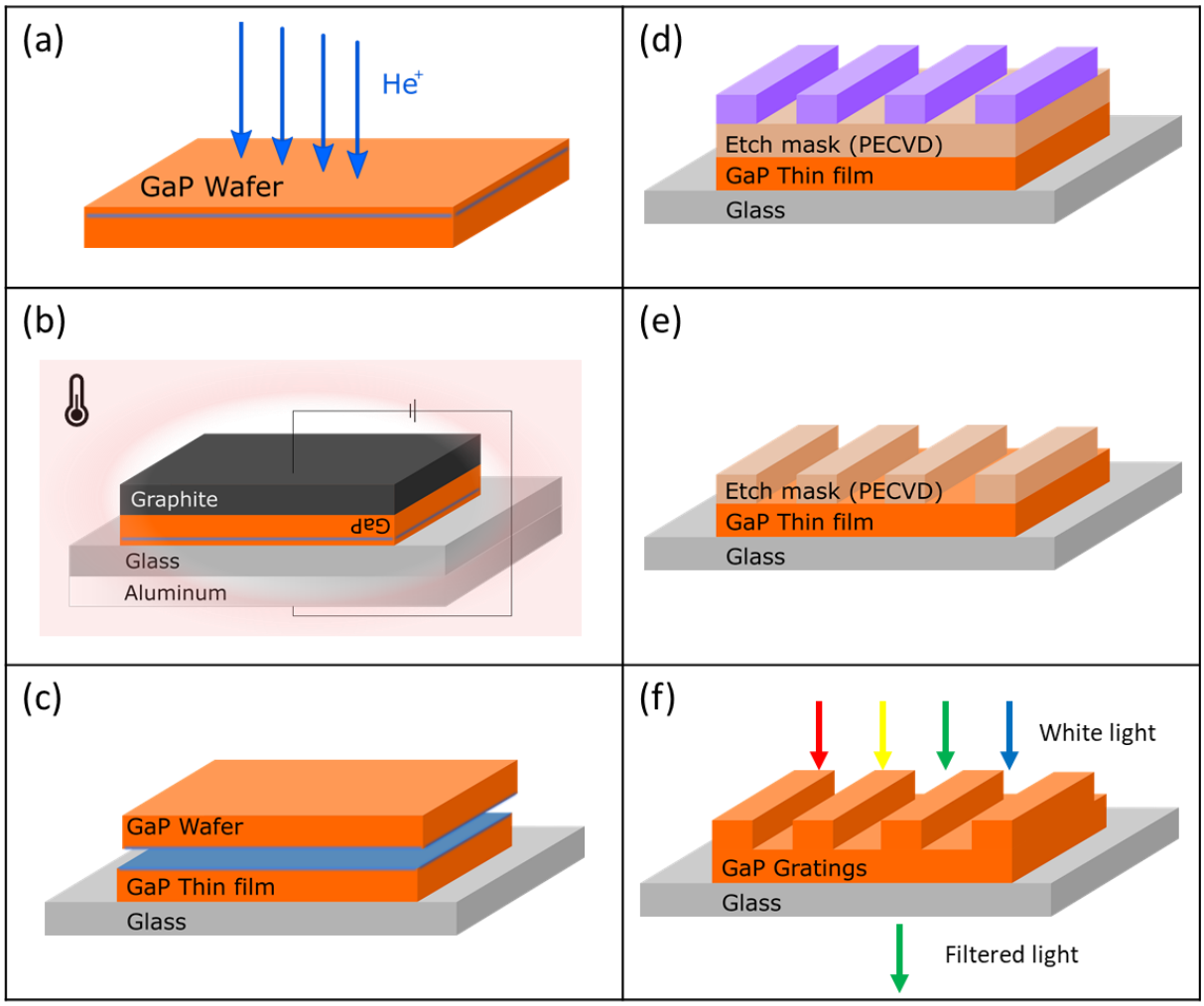

Figure 7: Fabrication outline for GaP on glass transmission GMR filter. (a) The GaP is ion implanted with He^+ to create a subsurface layer of GaP supersaturated with He. (b) The implanted side is anodically bonded to a glass wafer after which the He atoms congregate and exfoliate the GaP wafer (c), causing the wafer to separate from the thin film which is now bonded to the glass substrate. A hard-mask is deposited and (d) E-beam lithography is used to draw the grating pattern on the sample, which is etched into the hard-mask (e). Finally, a plasma etch is used to remove the hard-mask and get the finished devices (f).

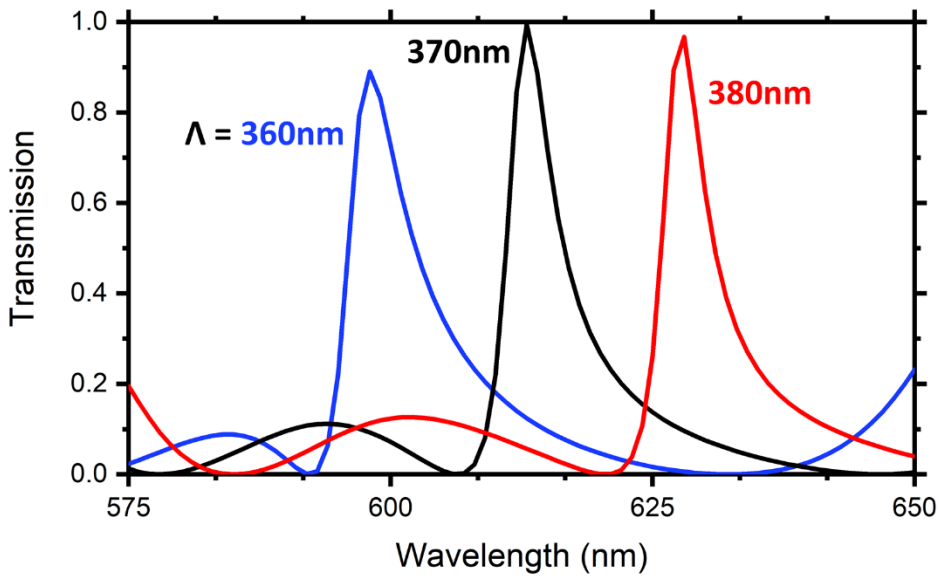

Figure 8: Showing how changing the increasing the grating period blue shifts the transmission peak. Above, three peaks are shown for D_g = 150 nm, D_F = 200 nm, and f = 58%. Notice how the peak shape is also slightly affected by period.

The objective of the design process is to develop a filter with a narrow transmission near 650 nm and little transmission in the nearby regions. The grating design process begins by simulating a grating with a period Λ of 400 nm and trying various values of D_g, D_f and f in search of a combination for which a transmission peak is obtained between 600 nm and 700 nm.

The transmission for various values of D_g, D_f and f and can then be plotted and peaks of high transmission surrounded by regions of low transmission can be searched for. Once D_g, D_f and f are selected, Λ can be adjusted to fine tune the peak location to the desired wavelength (Figure 8). Note that this method of fine tuning only works for shifting the peak location over short distances, since the peak will begin to diminish in prominence as the change in period becomes very large. This method can be repeated in any wavelength range to design a variety of devices.

For this work, the selected grating geometry had been simulated in previous work, to give D_g = 176nm, D_F = 106nm, f = 49% and Λ = 439 nm. These properties gave the transmission profile shown in Figure 9.

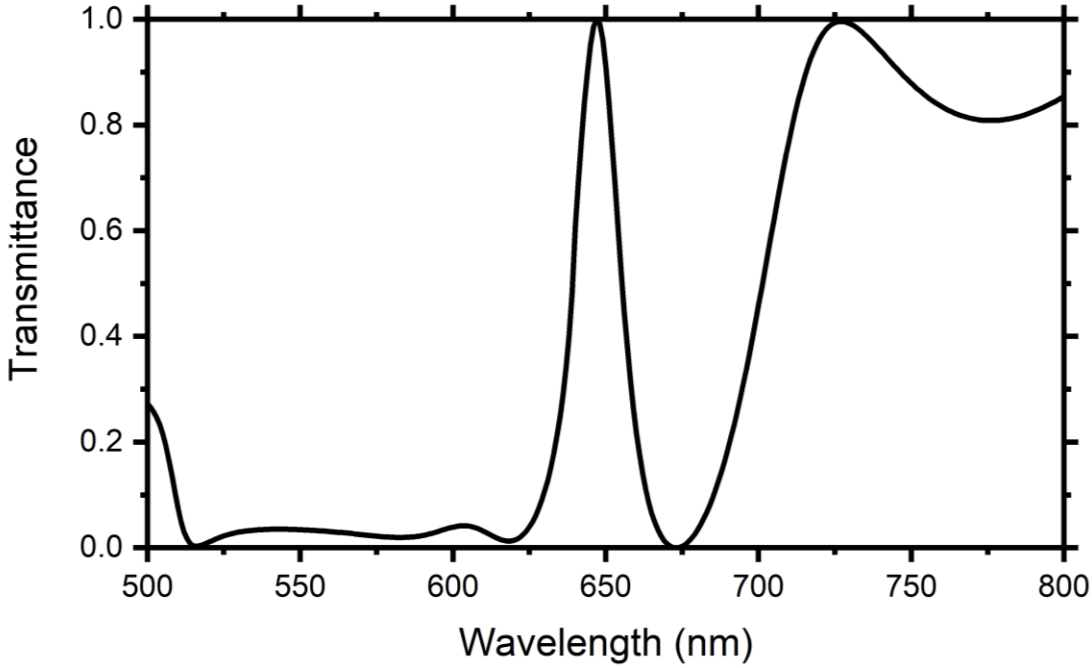

Figure 9: Simulated grating transmission spectra at optimized grating design.

3.2 Layer Transfer

The layer transfer process described in this work rests on two processes. The first is anodic bonding or field assisted thermal bonding, which is used to affix the gallium phosphide thin film to glass. The second is ion implantation, which is used to create a subsurface region of GaP supersaturated with helium. Section 3.1.1 explains anodic bonding theory and Section 3.1.3 does the same for ion implantation and exfoliation. Section 3.2 uses the facts discussed in Sections 3.1.1 and 3.1.3 to arrive at fabrication parameters.

3.2.1 Anodic Bonding Theory

Wafer bonding techniques are commonly used in the world of silicon-on-insulator devices and in the fabrication of silicon based micro-electro-mechanical systems. These techniques employ the van der Waals forces that dominate intermolecular interactions over short distances by brining two well-polished surfaces together. When this is done with two semiconductors or a semiconductor and a glass at room temperature, a bond is formed that holds the surfaces together and resists separation. However, such bonds can usually be broken with little force, making them unsuitable for permanent fixtures. By forming these bonds and then annealing at high temperatures for extended periods of time, these bonds can be strengthened.

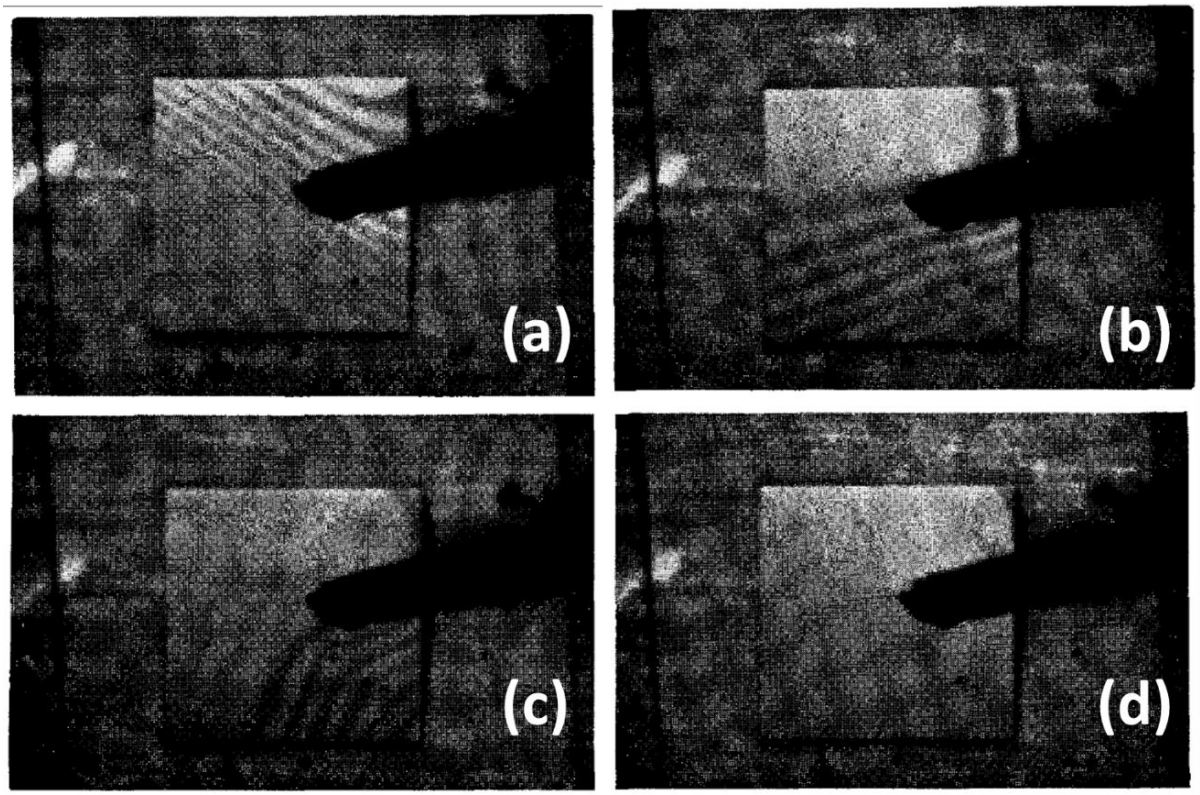

Figure 10: Micrographs of silicon-Pyrex interface taken during bonding process by Wallis and Pomerantz [14]. The black point is the wire connected to the glass to pass the high voltage. (a) through (d) demonstrate how the bond progresses outward from the primary point of contact.

This bonding process usually requires high temperatures, near the softening point for the glasses involved. This is because, even for well-polished surfaces, there will be micro-roughness that reduces the surface over which the two layers are contacting. Heating the glass and thereby increasing its softness can cause it to deform around this micro-roughness and restore the lost contact-area, increasing the strength of the bond. However, such high temperatures are unacceptable for bonding finished devices since higher temperature can mobilize dopants in silicon and destroy devices. Additionally, differences in thermal expansion coefficients can create strain across the bond interface once the bonded materials are cooled, which can result in warping and a weakening of the bond. For these reasons, lower temperature bonding methods are desirable.

In 1969, Wallis and Pomerantz [19] first published a “field-assisted” bonding technique that they demonstrated created strong bonds between glasses and metals and even glasses and semiconductors at temperatures in the 300 °C to 600 °C range. They were able to show successful, void-free bonding at temperatures far below the softening point of the glass involved. This was because the applied voltage across the surface resulted in the diffusion of mobile positive ions in the glass, which created a space charge

region and a field across the bonding interface. When set up correctly, the field across the interface pulled the two surfaces together. Most conveniently, the attractive force was not uniform: it was highest around the edges of where the two surfaces contacted so that the contact area would spread outwards from every point of contact, as can be seen in Figure 10. This pushed air from between the two surfaces and significantly reduced the prevalence of voids, even when bonding was done at atmospheric pressures, for smaller samples.

Kanda et al. [20] further studied the bonding process and measured the current passing through the bonded material once it had reached the bonding temperature. They saw that, for the most part, the current passing through the interface would start out at a maximum and reduce monotonically in a way that agreed strongly with the equivalent circuit suggested by Wallis (Figure 11). To first approximation, the current draw looks like that of a capacitor (C0) in series with a resistor (R0). This makes sense if we think of the charge carriers in the glass, which are mostly mobile Na^+ ions, as experiencing resistance as they move through the glass medium and developing a capacitance in the form of the space charge region forming at the bond interface.

Dural and Romalis [21] bonded gallium phosphide to the ends of a Pyrex glass tube using an anodic bonding process to get a resilient bond. At a bond voltage of around 1500 V, a temperature of 218 °C and a pressure of 10 kPa, the bond current dropped to zero after two hours at the bond temperature. The bond was found to be hermetically tight, with negligible leakage found when tested with a He leak detector.

While the vanilla thermal bonding requires prohibitively high temperatures for III-V materials, which tend to become unstable above 500 °C [22], field assisted thermal bonding occurs at significantly lower temperatures, which allows for its extension to III-V materials. This fact is crucial for the device suggested in this thesis, since crystalline GaP would be very difficult to deposit on amorphous substrates like most glasses. Consequently, a wafer bonding technique that can fix GaP to glass simplifies the fabrication of this device.

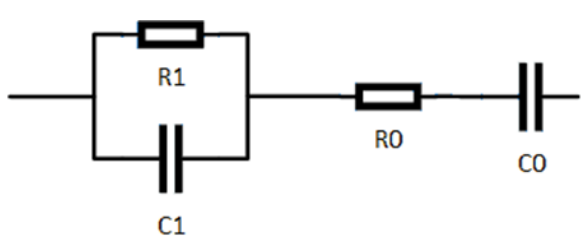

Figure 11: Equivalent circuit suggested by Wallis for bonding process, used by Kanda et al. [15]

3.2.2 Past Work in Anodic Bonding

There exist numerous examples of silicon to glass anodic bonding, mostly to Pyrex glass [23], but most form strong, near instantaneous bonds, even at ambient pressure and temperatures under 500 °C. For instance, Roylance and Angell [24] fabricated silicon-on-glass accelerometers using an anodic bonding technique that involved pressing etched silicon devices against a glass substrate at 400 °C with a bond voltage of 600 V. In a similar process using the same bonding parameters, Terry et al. [25] bonded a 5 cm diameter silicon wafer to a Pyrex glass sheet and note that, once at the bonding conditions, the bond is formed nearly instantaneously.

However, in their review on anodic bonding, Knowles and van Helvroot [23] note that anodic bonding to glass usually involves the formation of some oxide on the bond interface linked to the material being bonded to glass, and the quality of this oxide greatly affects the properties of the bond. They point out that molybdenum, for example, readily forms an oxide which allows for quick bonding, but the brittle nature of the oxide weakens the bond, unless special care is taken. One such measure is noted by Wallis [26], involving applying the bond voltage before heating, which gives time for air trapped at the interface to be pushed out by the electrostatic attraction and reduce the oxidation of the molybdenum.

More interestingly, Hök et. al. [27] demonstrated anodic bonding of gallium arsenide to glass. The bond was carried out at a temperature of 360 °C and a voltage of 800 V. It was noted that the space charge took 5-10 minutes to build up, with the bond being completed after 30 minutes. While initial attempts were prone to failure due to the formation of a weak gallium oxide at the bond interface, they were able to mitigate the issue by purging the glass of oxygen containing complexes by annealing it in a reducing atmosphere (H_2 and N_2) at 400 °C for 15 hours.

3.2.3 Ion Implant and Exfoliation

Ion implantation is a very common technique used to introduce impurities very precisely into a target substrate. It involves generating a gas of ions of a chose element, which are then accelerated through a high voltage circuit into a substrate. This is usually immediately followed by an annealing phase, since ions with a large kinetic energy can break bonds and displace atoms during the implantation process, which is especially damaging for crystalline substrates. The main parameters affecting the ion implant are the kinetic energy and mass of the incident ions and the chosen angle of incidence.

As ions arrive at the surface and begin to move through the material, they eventually collide with substrate atoms. During these collisions, they lose energy and are deflected, with the angle of deflection increasing as the ion loses kinetic energy or if the ion is massive. Additionally, if the energy imparted is

high enough, then the collision could displace a substrate atom, creating defects. This implant damage also increases as a function of implant energy and ion mass. Over a large substrate, a fair assumption is that these phenomena occur randomly, so that stochastic implementations like in the widely used Stopping Range of Ions in Matter (SRIM) software package [28] used in this work are often effective simulations. These simulations assume that the substrate is a random mixture of substrate ions and track the path of many ions impinging the surface, assuming random collisions where the probability of colliding with a substrate atom is independent of any previous collisions and is proportional to the atomic ratio of that atom in the substrate.

Using these methods, the ion implant profile can be calculated for various source ions, implant energies and implant angles. While higher angles increase the amount of energy required (and hence the implant damage) to get ions deep into the substrate, they also increase the apparent randomness of the lattice to the incident ions. This is because a highly ordered crystal will have some faces along which incident ions will be channeled, resulting in significantly deeper implantation than in the simulation. Increasing the angle of incidence slightly above 0°, usually as little as 1-2°, is seen in the literature to be sufficient to prevent channeling.

Another useful property of ion implantation is that it is a non-equilibrium process. This means that it can be used to infuse a substrate with an impurity concentration that exceeds that impurity's solubility in the substrate. From thermodynamics, we know that such a solid is only meta-stable, in that its constituents will eventually phase separate into a solid phase (which is the substrate saturated with the impurity) and an impurity phase (which is the impurity saturated with the substrate). In the case of GaP supersaturated with He, the two phases are GaP saturated with He and He bubbles that are formed inside GaP. Additionally, since the rate of this process is dependent on the diffusion rate of He in GaP, it increases exponentially with temperature.

By intentionally subjecting the GaP substrate to a high dose of He, a supersaturated layer of He in the GaP is formed. When this GaP is heated during anodic bonding, the He in the GaP is mobilized, forming a layer of bubbles that severely exfoliate the GaP in a localized layer of uniform depth, causing the substrate to separate from a thin film left bonded to glass.

While this technique has been demonstrated for pairs of materials other than silicon and glass, it has not before been demonstrated on GaP. Kim et al. [29] have demonstrated the layer transfer process to make Ge-on-insulator devices, noting that the mismatch between the thermal expansion coefficients of germanium and silicon made the films crack in early trials. They were able to solve this issue by bonding smaller samples.

Layer transfer of InAs onto a dielectric thin film was demonstrated by Sumita et al. [30]. In their work, the InP surface was covered with a PECVD SiO_2 layer before ion implantation. In the works of both Radu et al. (transferring GaAs onto insulator) [31] and Cioccio et al. (transferring GaAs and InP onto insulator) [32], an intermediary SiO_2 layer is first deposited on the transferred material surface, since III-V oxides tend to not be as resilient. In both works, hydrogen implantation was used to weaken the surface and blistering was observed on the sample surface, even before the annealing process.

3.3 Implant and Bonding Parameters

The objective was to leave a 500 nm thick film of GaP on the glass surface, which exceeds the requirement of the design, so that any roughness resulting from the exfoliation process could be removed by polishing. For this reason, a projected range of about 500 nm was chosen and SRIM suggested an implant energy of about 90 keV at normal incidence. Using this estimation and several transport of ions in matter (TRIM) simulations, it was determined that an implant energy of 92 keV was desired at an incident angle of 7° to obtain a projected range of 500 nm. A dose of 5E17 cm^{-2} was used to get a peak He concentration exceeding 1E21 cm^{-3} (Figure 12). It was later found that the surface roughness was minimal, so, in the next batch of implanted material, an implant energy of 47 keV was used, with a dose of 4.15E17 cm^{-2}.

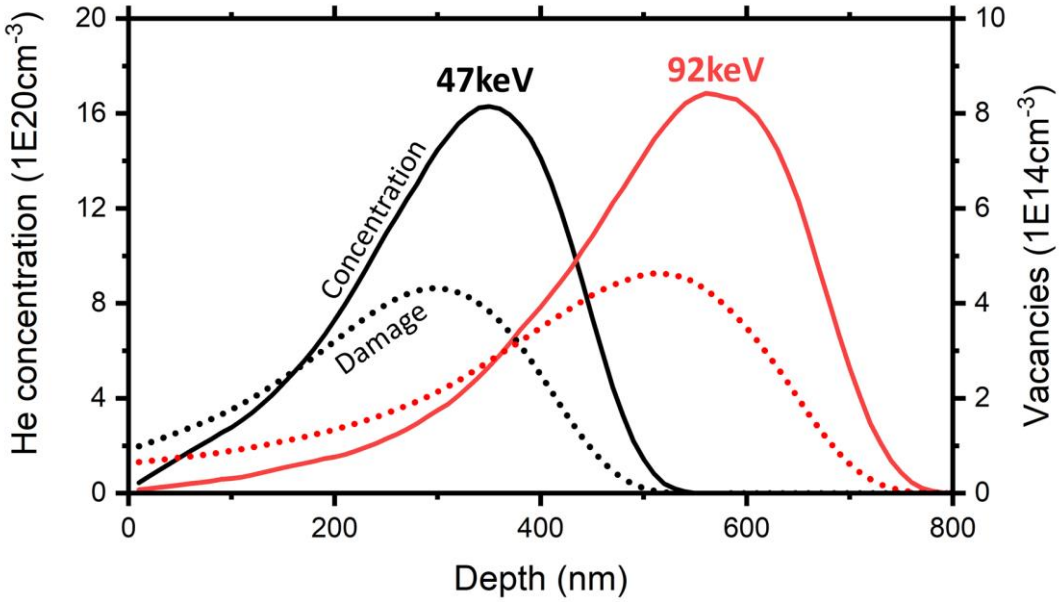

Figure 12: Simulated ion implant profile for He in GaP, at an incident angle of 7°. The red lines represent the 92 keV implant and the black lines represent the 47 keV implant. The solid lines represent the He concentration (left axis) and the dotted lines represent the vacancy concentration (right axis).

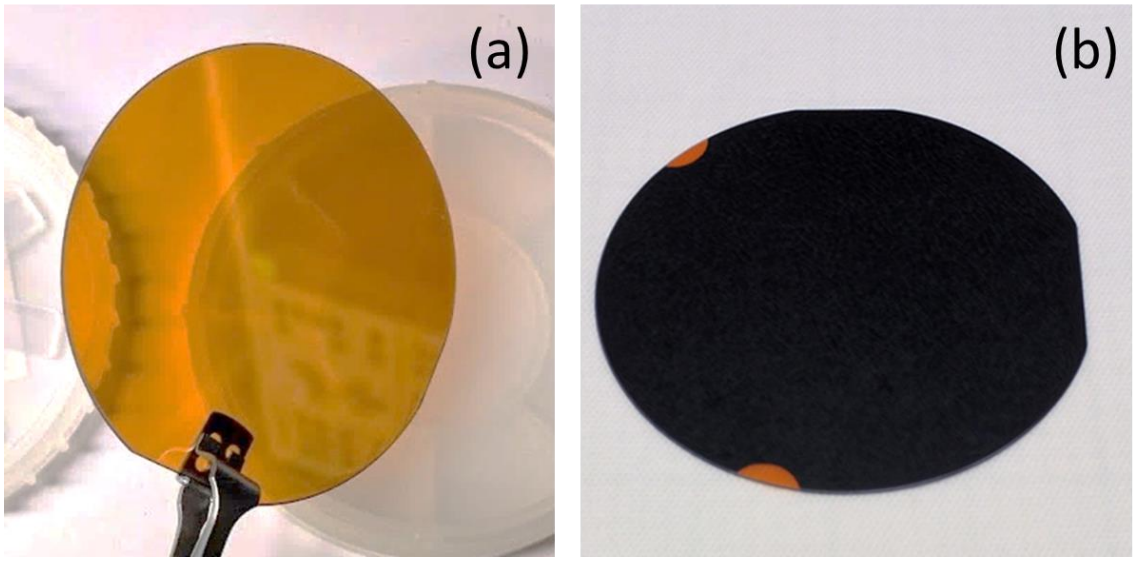

Figure 13: GaP wafer before ion implantation (a) and after ion implantation (b).

Interestingly, these samples did not blister, like in previous works [31], [32]. It is possible that the helium did not separate from the GaP as easily as the implanted hydrogen did, due to its larger atomic size.

The wafer (50.0 mm n-type GaP) was then cleaved in 5 mm x 5 mm squares. A sheet of borosilicate glass (n-BK7) was procured and diced into squares of dimension 12.5 mm x 12.5 mm. Before bonding, these samples were rinsed using, in order, acetone, isopropyl alcohol, water and isopropyl alcohol. They were then placed in an oxygen RF plasma at 75 W for 60 seconds, to clean any residual organics from the surface.

Despite the success off Dural and Romalis [21] at low temperature bonding, initial anodic bonds in this work were carried out at 400 °C and 1000 V (applied at the side of the GaP sample) since the EVGA 501S being used to anodically bond could not access higher voltages without arcing. The bonding chamber was pumped down to 10 Pa before the voltage was turned on and the samples were pressed down with 500 MPa of pressure. The sample was then heated to 400 °C in approximately 10 minutes, where it was held at temperature for 1 hour to allow for the formation of the space charge region. It was cooled to 150 °C, to reduce the mobility of the ions in the glass before the voltage was turned off. The vacuum was then vented, and the sample was cooled to room temperature. Upon removing the samples from the chamber, the GaP substrate would readily slide off the glass, leaving a smooth, square thin film of GaP in the imprint of the square samples used.

3.3.1 Results of Layer Transfer

After ion implantation, the orange GaP wafers had turned dark (Figure 13), possibly because of extensive implant damage resulting from the high dose implant. It is possible that this is due to the significant implant damage suggested by the simulation (Figure 12).

Because both glass and GaP are transparent, the quality of the bond formed was usually visible from the presence and density of fringe patterns visible both by eye and using a low-power microscope. Similar to Wallis [19], a high density of fringes implies that the materials are not well bonded. To qualitatively analyze bond strength, the sample was bent by pressing with tweezers and examining for shifts in fringe patterns. When fringe patterns shifted greatly, it was clear that the two surfaces were not deforming together (Figure 14).

When bonding, it was found that the most noticeable differences in bond quality resulted from varying the size of the samples being bonded and the bonding temperature. Tests were initially done bonding 10 mm x 10 mm GaP samples and 22.5 mm x 22.5 mm glass squares, but these tended to crack during the bonding process. It was suspected that the bond chuck deformed slightly during bonding resulting in an uneven exposure of pressure (which was confirmed using a pressure sensitive indicator film). To alleviate this issue, smaller samples were used, which also tended to give better bonds. Bonds were also run at temperatures lower than 400 °C and, as expected, the peak bond current and the current decay rate dropped as the temperature decreased Figure 15.

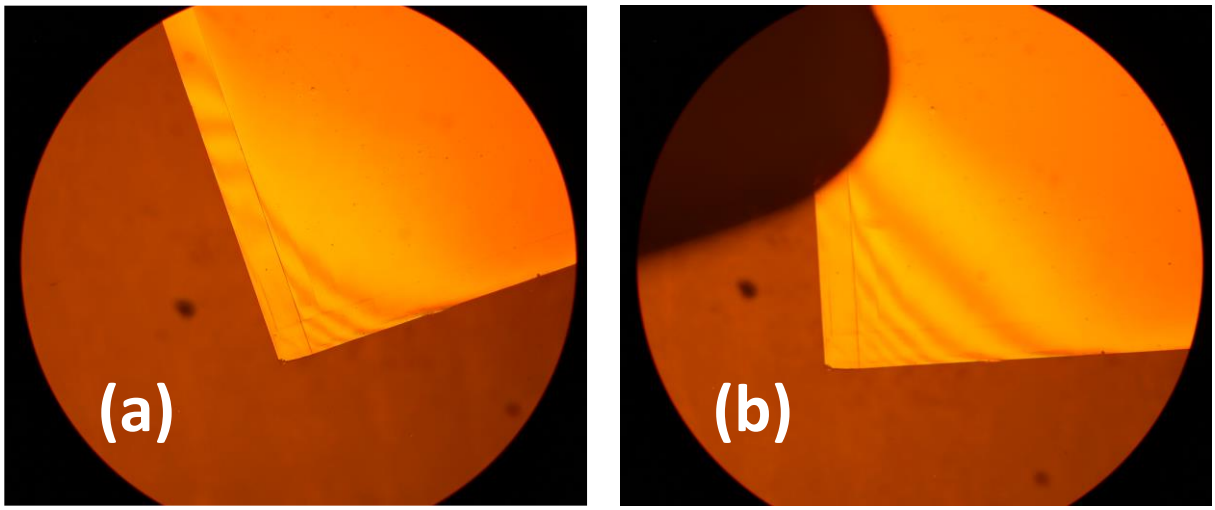

Figure 14: Microscope image of bulk GaP piece bonded to glass. (a) Fringe lines without pressure. (b) Fringe lines expanding when pressure is applied by tweezer.

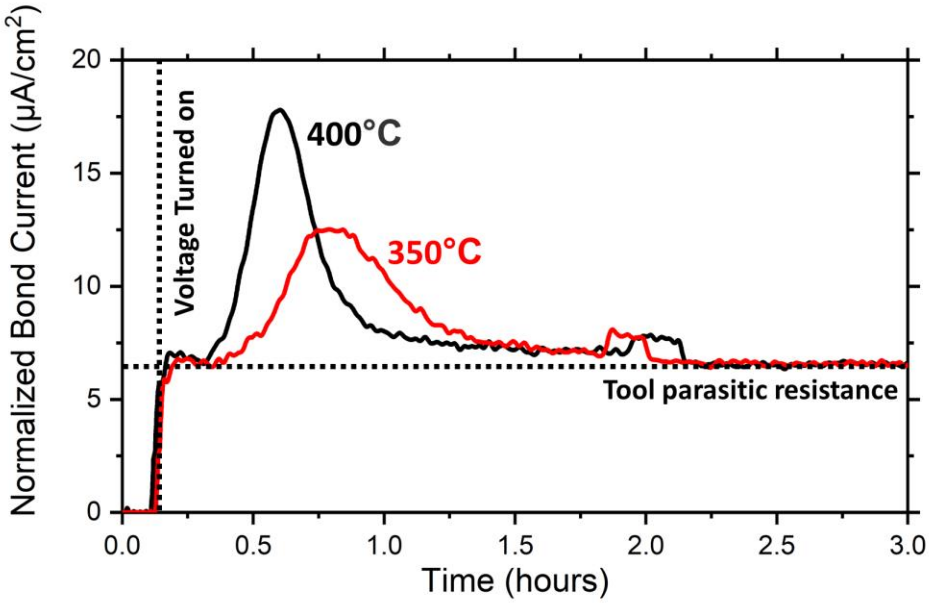

Figure 15: Area normalized bond current plotted vs. bond temperature. The sample heater is turned on just as the voltage is turned on. The initial rise in current results from the increasing mobility as the sample heats up. The current starts to drop as the space charge region forms a countering voltage.

A stylus profilometer was used to measure the step height from the glass surface onto the transferred GaP thin film near the edge of the square film. For the 92 keV implant, thicknesses averaging 707 nm were measured, with a standard deviation of 6 nm while, for the 47 keV implant, thicknesses averaging 396 nm were measured, with a standard deviation of 6 nm. Both these values are considerably larger than expected, based on the peak concentration values in each substrate.

The rms surface roughness was measured using atomic force microscopy to be ~10 nm, which was deemed to be smooth enough that further polishing was not required. Instead, the sample was thinned using a 3:1:1 solution of H_2O:H_2SO_4:H_2O_2, at 50°C (with an etch rate ~60 nm/min) to bring the sample thickness down to the desired thickness. It was confirmed that the solution did not measurably etch (<10 nm) the borosilicate glass, even after 10 minutes, so the height of the GaP thin film was determined by measuring the step height at the edge of the film. Interestingly, post-thinning, the sample surface seemed to be pockmarked with voids, which seemed indicative of the exfoliation process (Figure 16).

3.4 Etching of Gratings

All gratings were etched using either a silicon oxide hard mask (deposited using PECVD) or a silicon nitride hard mask (deposited using mixed frequency PECVD) of various thicknesses. The gratings were patterned using an E-beam lithography system.

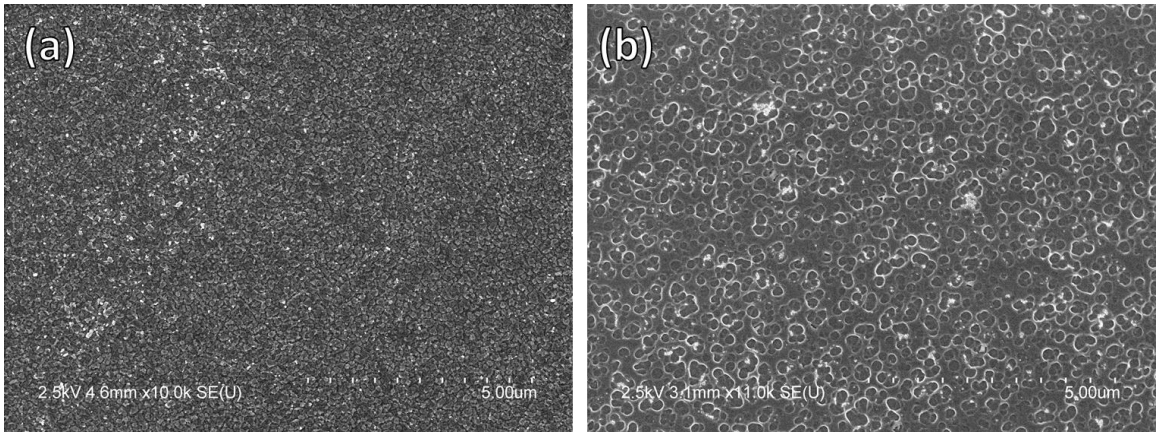

Figure 16: SEM image of GaP thin film surface after layer transfer and before (a) and after (b) wet etching. After wet etching, void like structures can be clearly seen.

For the first iteration of devices, a thin layer (~50 nm) of PECVD silicon oxide was used as a hard mask. The pattern from the lithography was transferred into the hard mask using an Oxford Instruments ICP RIE etcher, with an RIE power of 500 W and an ICP power of 1500 W. The chamber pressure was maintained at 10 mT and the etching gas was pure trifluoromethane pumped in at a flowrate of 40 sccm. This etch was found to etch the hard mask at a rate of ~70 nm/min while etching the GaP thin film at a rate of ~6 nm/min, giving a selectivity of ~12:1, with a preference for the hard mask.

The resist was cleaned off by soaking in PG remover for 1 hour, followed by washing with acetone, isopropyl alcohol, water, and isopropyl alcohol in that order. This was followed by an O_2 plasma "descum" to remove any residual organics from the surface. The samples were then etched in an Oxford Instruments ICP RIE etcher, using no ICP power and an RIE power of 80W. The pressure was reduced to 4 mT, which is as low as the system would go without introducing instability, and the etch gasses BCl_3 and Cl_2 were pumped into the chamber at flowrates of 5 sccm each (Figure 17 a). This process was found to have a selectivity of ~20:1 with a preference for the hard mask, so only a small amount of hard mask was needed even for deep etching. However, the etch rate was high, at ~320 nm/min, which meant that very short etches would have to be used to get the desired etch depth of 176 nm. Additionally, this etch produced a profile with significant undercutting, which was undesirable.

To address the issues faced in the previous process, O_2 was added to the mixture of etch gasses. The addition of O_2 [33] has been shown to reduce the concentration of Cl^- ions in the plasma, which reduces the etch rate, and reduces undercutting. The next batch of samples was prepared with hard mask in a manner identical to the previous batch. The samples were then etched in the same ICP RIE etcher, with no ICP power and an RIE power of 80W. The pressure was kept at 4 mT and the etch gases used were BCl_3 and

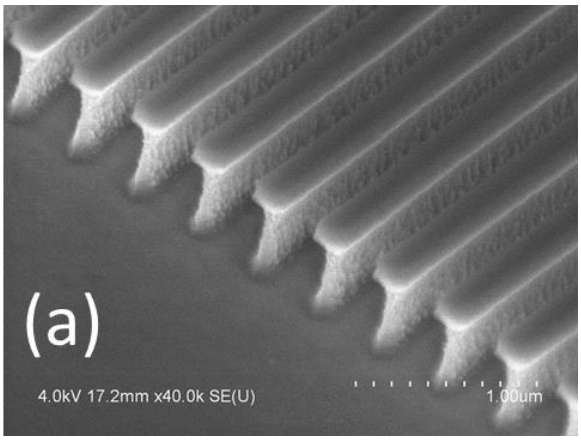

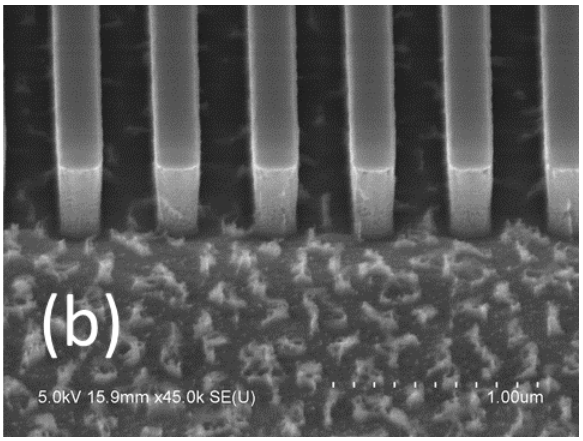

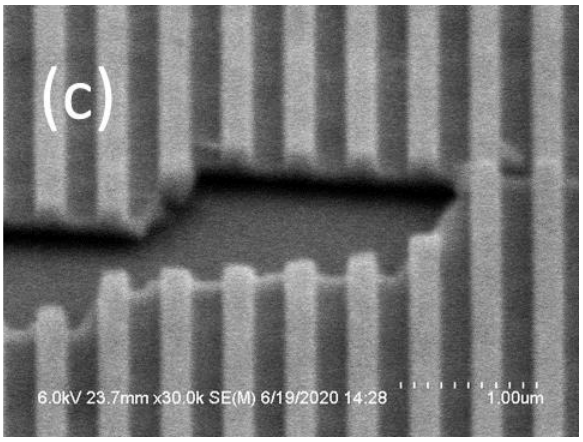

Figure 17: SEM showing etch profile for various etch chemistries. (a) BCl_3 and Cl_2 etch with clean floor but severe undercut. (b) BCl_3, Cl_2 and O_2 etch with vertical sidewalls but rough floor. (c) BCl_3, Cl_2, CH_4 and H_2 etch with vertical sidewalls and smooth floor.

Cl_2 pumped at 5 sccm each, and O_2 pumped in at 7 sccm (Figure 17 b). This etch differed from the last in that it was slower, with an etch rate ~180 nm/min, and had almost no undercutting as evidenced by the SEM images. While the etch had an even higher selectivity against the mask, at 36:1, this resulted in a roughening of the floor because of micro masking.

Since the floor was quite rough and the etch rate was still relatively high, a third etch recipe was attempted. Instead of diluting the etch gasses with O_2, the etch gasses were diluted with H_2 and CH_4. The hydrogen and methane mixture is supposed to polymerize in the plasma and deposit an etch retarding film over exposed surfaces on the sample. These films are supposed to be resilient to chemical etching and only come off when they are sputtered by ions accelerated by the chamber's generated DC bias, which encourages anisotropic etching.

Following the etch recipe described in [25], 80 W of RIE power and 600 W of ICP power. The gas flow rates included 10 sccm each of Cl_2 and BCl_3, 2 sccm of CH_4 and 17.5 sccm of H_2 (Figure 17 c). A stable plasma was achieved by striking at 7 mT and then rapidly lowering the pressure to 4 mT. Under these

conditions, an etch rate of 80 nm/min was measured. However, a significant increase in the etch rate for the hard mask resulted in a lowering of selectivity to 2:1. However, the lowered selectivity resolved the micro masking issue and restored smoothness to the etch floor.

It should be noted that, through the fabrication process, it was observed that the etches would significantly speed up as the etch progressed. This behavior was not as significant on similar tests performed on gratings etched into bulk GaP samples. It is suspected that, when etching thin film as opposed to bulk GaP, the surface gets significantly hotter because the glass substrate is less thermally conductive than GaP. This conjecture agrees with the observation that thinner films etched faster in the same etch conditions.

3.5 Transmission Spectra of Fabricated Gratings

Before measuring the transmission spectra, the area around the etched gratings was covered with a thin layer of evaporated metal, to ensure only light passing through the gratings was analyzed. The transmission spectra were measured using a Varian Cary 5G spectrophotometer (Figure 18). Since the transmission characteristics of GMR gratings are dependent on the polarization of the incident light, a linear polarizer was put in the beam path before the GaP gratings so that the E-field was polarized perpendicular

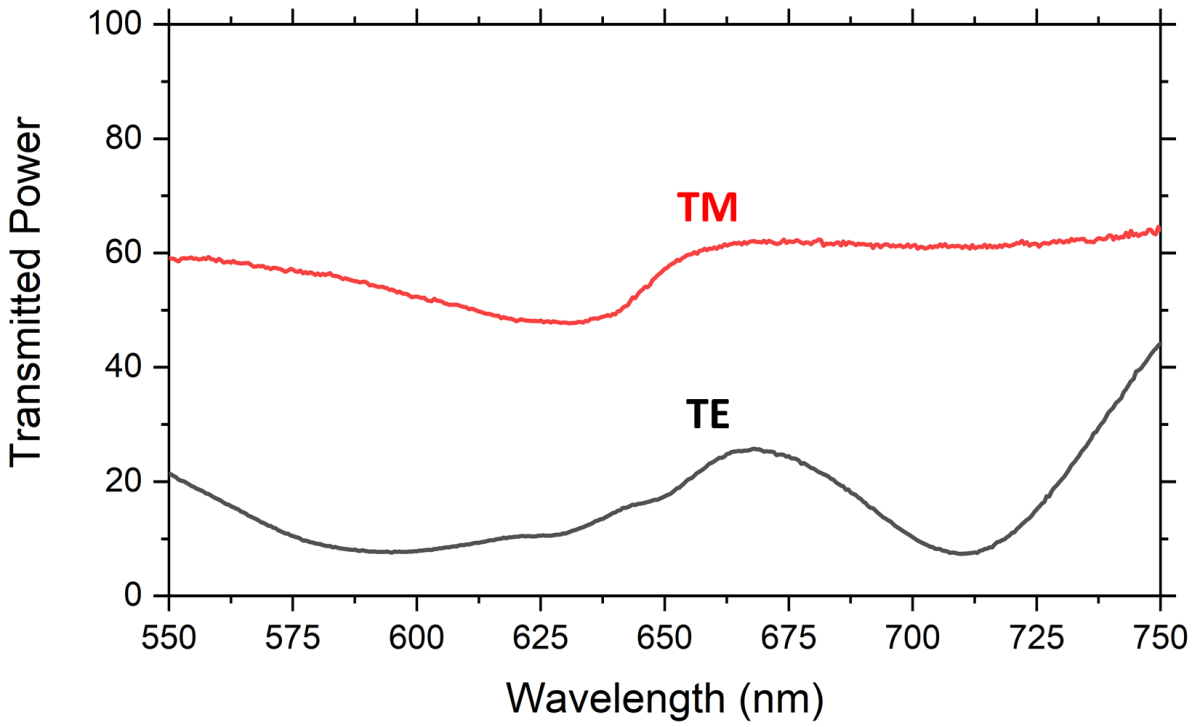

Figure 18: Transmittance profile of fabricated GMR gratings for different polarizations of incident light.

to the gratings (s-polarized according to Figure 1). A baseline measurement was taken without the grating in the path, to normalize out the transmission of the filter.

As can be seen, the transmission spectrum presents a peak that is far broader and shorter than expected. This is suspected to be a consequence of the sensitivity of the grating design to minor changes in the fabrication parameters.

CHAPTER 4

CONCLUSION AND FUTURE WORK

A useful technique for the preparation of thin films on non-native substrate via ion implantation and exfoliation is demonstrated. This technique is shown to produce films of consistent quality and low surface roughness, though more work needs to be done to link the ion implant profile with the resulting thin film thickness. This technique does result in a significant change in the optical absorption of the material and more work needs to be done to determine if the optical properties of the film have been significantly altered.

The GMR transmission filter design suggested above does not seem to perform as well as hoped. Since only one device was fabricated fully and tested, it is possible that repeated attempts would achieve better transmission spectra. In subsequent attempts, extra caution should be taken, when etching the gratings into the GaP, to try and more precisely hit the targeted etch depth.

Another possible mode of failure could be the low tolerance of the grating design for errors in fabrication. It might be more fruitful to try an alternate approach that is less sensitive. One possible pathway could be to use evaporated metal gratings instead of etched gratings, as was done by Song et al. [13]. This method allows for an increased reflectance of the base thin film stack, due the high extinction coefficient in the metal film, if a large fill factor is used. The use of layer transferred GaP as a waveguide, instead of the dielectric stack used by Song et al., should improve the confinement factor of the guided mode and reduce ohmic losses. While ohmic losses would persist, the gains in the quality of the background when compared to the design studied in this work should justify such a tradeoff.

REFERENCES

[1] Y. Wan *et al.*, "Compact characterization of liquid absorption and emission spectra using linear variable filters integrated with a CMOS imaging camera," *Sci. Rep.*, vol. 6, no. 1, pp. 1–9, Jul. 2016, doi: 10.1038/srep29117.

[2] E. Engvall and P. Perlmann, "Enzyme-linked immunosorbent assay, Elisa: III. Quantitation of specific antibodies by enzyme-labeled anti-immunoglobulin in antigen-coated tubes," *J. Immunol.*, vol. 109, no. 1, pp. 129–135, Jul. 1972.

[3] R. I. Seddon, B. L. Swaby, R. J. Ryall, S. E. Solberg, and E. W. Anthon, "Monolithic linear variable filter and method of manufacture," U.S. Patent No. 5,872,655A, Feb. 16, 1999.

[4] J. Yang, P. T. Lin, and P. T. Lin, "Real-time and non-destructive gas mixture analysis using linear various filter enabled mid-infrared visualization," *Opt. Express*, vol. 27, no. 19, pp. 26512–26522, Sep. 2019, doi: 10.1364/OE.27.026512.

[5] A. Hessel and A. A. Oliner, "A new theory of Wood's anomalies on optical gratings," *Appl. Opt.*, vol. 4, no. 10, pp. 1275–1297, Oct. 1965, doi: 10.1364/AO.4.001275.

[6] R. W. Wood, "On a remarkable case of uneven distribution of light in a diffraction grating spectrum," *Proc. Phys. Soc. Lond.*, vol. 18, no. 1, pp. 269–275, Jun. 1902, doi: 10.1088/1478-7814/18/1/325.

[7] Lord Rayleigh, "Note on the remarkable case of diffraction spectra described by Prof. Wood," *Lond. Edinb. Dublin Philos. Mag. J. Sci.*, vol. 14, no. 79, pp. 60–65, Jul. 1907, doi: 10.1080/14786440709463661.

[8] C. H. Palmer, "Parallel diffraction grating anomalies," *JOSA*, vol. 42, no. 4, pp. 269–276, Apr. 1952, doi: 10.1364/JOSA.42.000269.

[9] S. S. Wang, R. Magnusson, J. S. Bagby, and M. G. Moharam, "Guided-mode resonances in planar dielectric-layer diffraction gratings," *JOSA A*, vol. 7, no. 8, pp. 1470–1474, Aug. 1990, doi: 10.1364/JOSAA.7.001470.

[10] T. K. Gaylord and M. G. Moharam, "Analysis and applications of optical diffraction by gratings," *Proc. IEEE*, vol. 73, no. 5, pp. 894–937, May 1985, doi: 10.1109/PROC.1985.13220.

[11] S. S. Wang and R. Magnusson, "Theory and applications of guided-mode resonance filters," *Appl. Opt.*, vol. 32, no. 14, pp. 2606–2613, May 1993, doi: 10.1364/AO.32.002606.

[12] Y. Kanamori, M. Shimono, and K. Hane, "Fabrication of transmission color filters using silicon subwavelength gratings on quartz substrates," *IEEE Photonics Technol. Lett.*, vol. 18, no. 20, pp. 2126–2128, Oct. 2006, doi: 10.1109/LPT.2006.883208.

[13] S. Song, F. Sun, Q. Chen, and Y. Zhang, "Narrow-linewidth and high-transmission terahertz bandpass filtering by metallic gratings," *IEEE Trans. Terahertz Sci. Technol.*, vol. 5, no. 1, pp. 131–136, Jan. 2015, doi: 10.1109/TTHZ.2014.2365679.

[14] C.-H. Park, Y.-T. Yoon, and S.-S. Lee, "Polarization-independent visible wavelength filter incorporating a symmetric metal-dielectric resonant structure," *Opt. Express*, vol. 20, no. 21, pp. 23769–23777, Oct. 2012, doi: 10.1364/OE.20.023769.

[15] R. Magnusson and S. S. Wang, "Transmission bandpass guided-mode resonance filters," *Appl. Opt.*, vol. 34, no. 35, pp. 8106–8109, Dec. 1995, doi: 10.1364/AO.34.008106.

[16] K. V. Srikrishnan, "Smart-cut process for the production of thin semiconductor material films," U.S. Patent No. 5,882,987, Mar. 16, 1999.

[17] M. Ganjoo, J. A. Carlson, S. A. Al-Mulla, J. Brown, B. T. Cunningham, and J. M. Dallesasse, "Transfer of thin film gallium phosphide onto glass for integrable optical filters," Tuscon, Arizona, May 2020, pp. 5–8, [Online]. Available: https://docs.omnibooksonline.com/assets/GMI12142/70377/70377_CSMANTECH_complete_book_4.pdf.

[18] M. G. Moharam and T. K. Gaylord, "Rigorous coupled-wave analysis of planar-grating diffraction," *JOSA*, vol. 71, no. 7, pp. 811–818, Jul. 1981, doi: 10.1364/JOSA.71.000811.

[19] G. Wallis and D. I. Pomerantz, “Field assisted glass-metal sealing,” *J. Appl. Phys.*, vol. 40, no. 10, pp. 3946–3949, Sep. 1969, doi: 10.1063/1.1657121.
[20] Y. Kanda, K. Matsuda, C. Murayama, and J. Sugaya, “The mechanism of field-assisted silicon-glass bonding,” *Proc. 5th Int. Conf. Solid-State Sens. Actuators Eurosensors III*, vol. 23, no. 1, pp. 939–943, Apr. 1990, doi: 10.1016/0924-4247(90)87064-P.
[21] N. Dural and M. V. Romalis, “Gallium phosphide as a new material for anodically bonded atomic sensors,” *APL Mater.*, vol. 2, no. 8, p. 086101, Aug. 2014, doi: 10.1063/1.4891375.
[22] I. Mojzes, B. Pécz, R. Veresegyházy, and B. Kovács, “Thermal decomposition of compound semiconductors covered with thin metallic layers,” *Period. Polytech. Electr. Eng. Arch.*, vol. 35, no. 4, Art. no. 4, 1991.
[23] K. M. Knowles and A. T. J. van Helvoort, “Anodic bonding,” *Int. Mater. Rev.*, vol. 51, no. 5, pp. 273–311, Oct. 2006, doi: 10.1179/174328006X102501.
[24] L. M. Roylance and J. B. Angell, “A batch-fabricated silicon accelerometer,” *IEEE Trans. Electron Devices*, vol. 26, no. 12, pp. 1911–1917, Dec. 1979, doi: 10.1109/T-ED.1979.19795.
[25] S. C. Terry, J. H. Jerman, and J. B. Angell, “A gas chromatographic air analyzer fabricated on a silicon wafer,” *IEEE Trans. Electron Devices*, vol. 26, no. 12, pp. 1880–1886, Dec. 1979, doi: 10.1109/T-ED.1979.19791.
[26] G. Wallis, “Field assisted glass sealing,” *Electrocompon. Sci. Technol.*, vol. 2, no. 1, pp. 45–53, 1975, doi: 10.1155/APEC.2.45.
[27] B. Hök, C. Dubon, and C. Ovrén, “Anodic bonding of gallium arsenide to glass,” *Appl. Phys. Lett.*, vol. 43, no. 3, pp. 267–269, Aug. 1983, doi: 10.1063/1.94322.
[28] J. F. Ziegler, M. D. Ziegler, and J. P. Biersack, “SRIM – The stopping and range of ions in matter (2010),” *19th Int. Conf. Ion Beam Anal.*, vol. 268, no. 11, pp. 1818–1823, Jun. 2010, doi: 10.1016/j.nimb.2010.02.091.
[29] M. Kim *et al.*, “Fabrication of Ge-on-insulator wafers by Smart-Cut^{TM} with thermal management for undamaged donor Ge wafers,” *Semicond. Sci. Technol.*, vol. 33, no. 1, p. 015017, Dec. 2017, doi: 10.1088/1361-6641/aa9bcd.
[30] K. Sumita, K. Kato, M. Takenaka, and S. Takagi, “Fabrication of thin body InAs-on-insulator structures by Smart Cut method with H^+ implantation at room temperature,” *Jpn. J. Appl. Phys.*, vol. 58, no. SB, p. SBBA03, Feb. 2019, doi: 10.7567/1347-4065/aafa68.
[31] I. Radu, I. Szafraniak, R. Scholz, M. Alexe, and U. Gösele, “GaAs on Si heterostructures obtained by He and/or H implantation and direct wafer bonding,” *J. Appl. Phys.*, vol. 94, no. 12, pp. 7820–7825, Dec. 2003, doi: 10.1063/1.1627459.
[32] L. D. Cioccio, E. Jalaguier, and F. Letertre, “III–V layer transfer onto silicon and applications,” *Phys. Status Solidi A*, vol. 202, no. 4, pp. 509–515, 2005, doi: https://doi.org/10.1002/pssa.200460411.
[33] R. H. Burton and G. Smolinsky, “CCl_4 and Cl_2 plasma etching of III–V semiconductors and the role of added O 2,” *J. Electrochem. Soc.*, vol. 129, no. 7, pp. 1599–1604, 1982.